2D Imaging of Sparse Array Radar in Rainy Scenes

Takuya Kawaguchi,[1] Kazuki Shinotsuka,[1] and Fumio Yajima[1]

In recent years, the demand for a millimeter-wave radar imaging has increased, therefore, a millimeter-wave radar with higher angular resolution has been highly expected. One of the solutions to achieve the higher angular resolution without increasing the complexity of the radar system is a sparse array radar. Generally, rain conditions are not considered in the verification of the sparse array radar performance, hence, an impact of the rain on the sparse array radar has not been clarified. For this reason, we designed and fabricated an in-house developed sparse array radar and experimentally verified the influence of the rain on the sparse array radar with several tests in a rain chamber.

1. Introduction

Advanced driver assistance systems (ADAS) are used to ensure the safety of drivers and other traffic participants, such as other vehicles, passengers and pedestrians. The ultimate goal of the ADAS is to create fully autonomous vehicles that can operate without driver control or monitoring. For the ADAS, sensors providing information to the autonomous driving control system are needed. Common sensors used in ADAS are ultrasonic sensors, millimeter-wave radars, LiDAR and cameras[1)]. Generally, ultrasonic sensors and millimeter-wave radars are used to measure distance and speed, while LiDAR and cameras are used for imaging purposes. However, optical sensors such as LiDAR and cameras experience a decline in sensing performance under adverse weather conditions such as rain or fog[2)-3)]. On the other hand, millimeter-wave radar is robust in adverse weather conditions, and recent studies have explored its use for imaging applications in such conditions[4)-6)]. However, conventional millimeter-wave radar has the issue of low angular resolution for imaging applications. The angular resolution of millimeter-wave radar is defined as[7)]:

$$\Delta\theta \approx \frac{\lambda}{D\cos\theta} \quad (1)$$

where λ is the wavelength, D is the array aperture, and θ is the angle from the radar boresight. Equation 1 shows that the higher angular resolution requires the larger array aperture. For a uniform linear array (ULA), which is a basic array configuration, increasing the aperture entails an increase in the number of antenna elements (Fig. $1a_1$, a_2). One method of suppressing this increase is the multiple input multiple output (MIMO) technique, which involves transmitting radio waves from multiple transmit antennas and receiving them with multiple receive antennas. Implementing MIMO radar makes it possible to increase the array aperture while suppressing the increase in the number of physical antennas[8)]. However, millimeter-wave radar imaging systems require higher angular resolution than conventional millimeter-wave radar systems. Thus, MIMO technology is not enough to reduce the number of antennas. For example, constructing a millimeter-wave radar imaging system with 1° angular resolution in both the azimuth and elevation directions using MIMO-ULA requires over 200 physical antennas. This leads to complex hardware configurations, increased signal processing loads, and higher system costs.

One of a possible solution for suppressing the increase in the number of antennas associated with array aperture expansion is sparse array antennas, which are antenna arrays in which the antenna elements are sparsely distributed. ULA antennas are arranged at equal intervals (Fig. $1a_2$), whereas sparse array antennas have larger spacing, and the elements are arranged at equal or unequal intervals (Fig. $1b_1$, b_2). The array configuration allows for the construction of an array with fewer physical antennas than a ULA with the same array aperture. Thus, sparse array antennas are a promising technique for enhancing the high-angular resolution of millimeter-wave radars[9)-11)]. However, an array whose the number of antenna elements is fewer than the one of ULA causes undersampling with respect to the field of view (FOV). This may result in aliasing, similar to a grating lobe. The aliasing degrades the system's signal-to-noise ratio (SNR) and consequently leads to degradation of output images. Various studies have addressed this issue, reporting that the aliasing can be suppressed through appropriate array design[9)]. However, no studies considering the influence of rainfall on aliasing occurrence have been identified. In millimeter-wave radar sensing, phase information of the received signals is critical, yet the phase is affected by rainfall. In the 76 to 81 GHz frequency band used for automotive long-range millimeter-wave radar[12)], the wavelength of the radio waves is around 3.7 to 3.9 mm, close to the average size of raindrops. Therefore, when the radio waves propagate under rainy conditions, they may scatter off raindrops. This scattering causes random changes in the phase and

1 : R&D Strategy Center

Abbreviations, Acronyms, and Terms.

ULA—Uniform Linear Array
An antenna array in which antenna elements are arranged at equal intervals of half wavelength

FOV—Field Of View
The angular extent of the observable area

FMCW—Frequency Modulated Continuous Wave
A method of transmitting a continuous wave of a specific frequency by modulating the frequency over a fixed period of time

RCS—Radar Cross Section
A measure of how well a target reflects radar signals back to the radar source

IF—Intermediate Frequency
The frequency obtained by mixing the transmitted signal and the received signal

DOA—Direction of Arrival
A direction from which a propagating wave arrives at a point where a sensor is located

Range Bin— —
The smallest unit on the distance scale

Radar Boresight— —
A direction perpendicular to the plane formed by a 2D antenna array

Undersampling— —
A state in which the sampling frequency is less than twice the maximum frequency contained in the signal

Aliasing— —
False signals

Grating Lobe— —
Side lobes of the same intensity as the main lobe

amplitude of the propagating radio waves[13] and may affect millimeter-wave radar sensing results. Here, since the sparse array antenna is in an undersampling state, the impacts of phase changes may be significant and lead to changes in aliasing and SNR degradation. Based on this, this study provides experimental verification results of the rainfall impacts on the sparse array radar. This verification was conducted by using an in-house developed sparse array radar, and the measurement results were obtained in an indoor test facility capable of imitating natural rainfall.

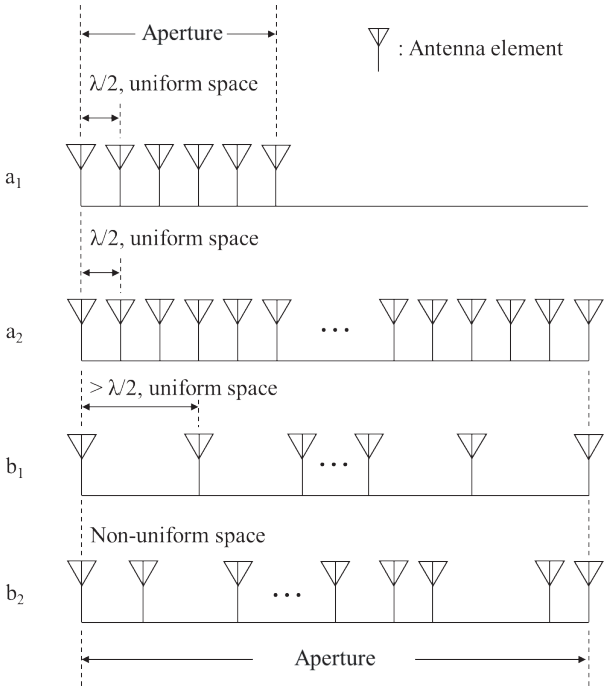

Fig. 1. (a_1, a_2) Antenna configurations of ULA, and (b_1, b_2) antenna configurations of sparse array.

2. Experiments

2.1 Rain chamber

As an indoor test facility capable of imitating natural rainfall, the large-scale rainfall experiment facility owned by the National Research Institute for Earth Science and Disaster Resilience was utilized. This facility is one of the world's largest and most advanced sprinkler systems capable of imitating conditions similar to natural rainfall[14]. The facility is 76 m in length, 49 m in width, and 21 m in height, with the ground surface paved with asphalt.

Before conducting experiments to verify the impacts of rainfall on a sparse array radar in this facility, experimental verification was conducted to check whether the facility could imitate conditions similar to natural rainfall. Regarding the particle size distribution of rain droplets in natural rainfall, Marshall and Palmer derived the experimental equation based on observational results[15]:

$$N_D = N_0 \cdot \exp(-\kappa \cdot D) \quad (2)$$

where N_D represents the number of raindrops, and D represents the diameter of the raindrops. N_0 is the value of N_D when D=0, and it is 0.08 cm^{-4}. κ is expressed as $41R^{-0.21}$, where R is the rainfall intensity in mm hr^{-1}. If the rain drop size distribution at this facility shows a trend similar to that in Equation 2, it can be said that this facility is capable of imitating conditions similar to natural rainfall. Figure 2 shows the rain drop size distribution measured by COTT-Parsivel-2 during the rain chamber was imitating rainfall of 50 mm hr^{-1}, and also the Marshall-Palmer distribution obtained by substituting R=50 in Equation 2. As shown in Fig. 2, the measured results and the Marshall-Palmer distribution show good correspondence. These results confirm that this facility can imitate a particle size distribution similar to natural rainfall. However, considering the

extremely heavy rainfall of 50 mm hr^{-1}, it is easy to imagine that sand and dust may mix into the rain in natural rainfall, and these particles could potentially affect millimeter-wave radar sensing. In this study, we present verification results considering the particle size, quantity, and distribution of raindrops without accounting for these factors.

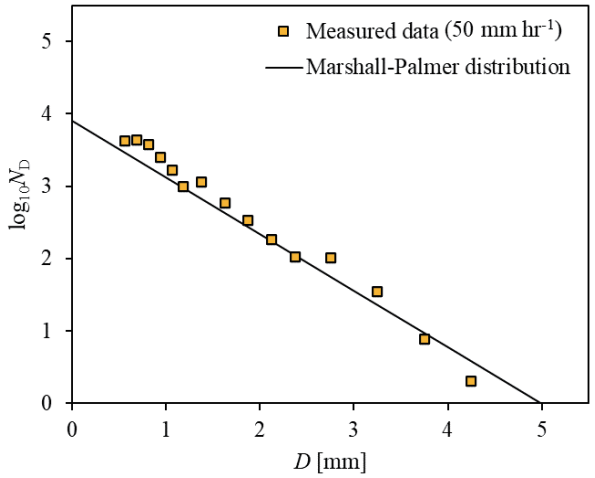

Fig. 2. Measurement results of the raindrop size distribution at 50 mm hr^{-1} rain (orange squares), and the Marshall-Palmer distribution for R=50 (black solid line).

2.2 Sparse array radar

The appearance of the sparse array radar used for the verification is shown in Fig. 3. This sparse array radar consists of four millimeter-wave radar ICs (AWR2243, Texas Instruments) connected in cascade. Each IC can utilize three transmit antennas and four receive antennas, resulting in a system with a total of 12 transmit antennas and 16 receive antennas. By utilizing all antennas as a MIMO radar, the radar can generate 192 virtual antennas. The AWR2243 is capable of generating FMCW signals, enabling the sparse array radar to function as an FMCW radar. The antenna spacing is designed to be 1.5λ, and the system has a 2D array configuration as shown in Fig. 4. Compared to a ULA with the same array aperture, this sparse array radar achieves the same angular resolution with 86 fewer antenna elements. The specifications of this sparse array radar are shown in Table 1. Initial performance evaluation results confirmed that the absolute error in the range direction is less than ±4 cm and the absolute error in the azimuth direction is less than ±0.5°.

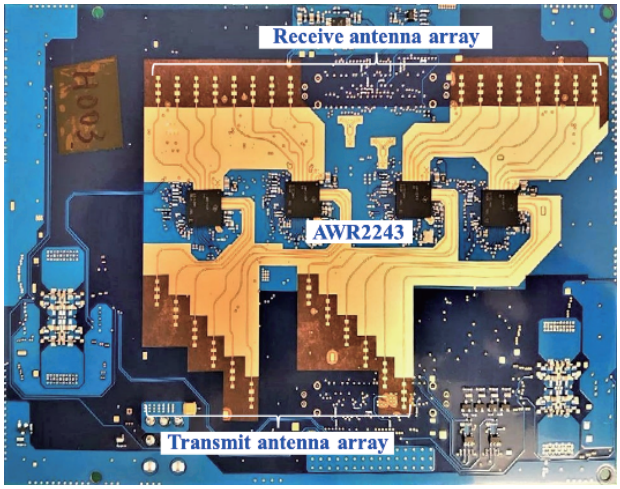

Fig. 3. Appearance of the in-house developed sparse array radar.

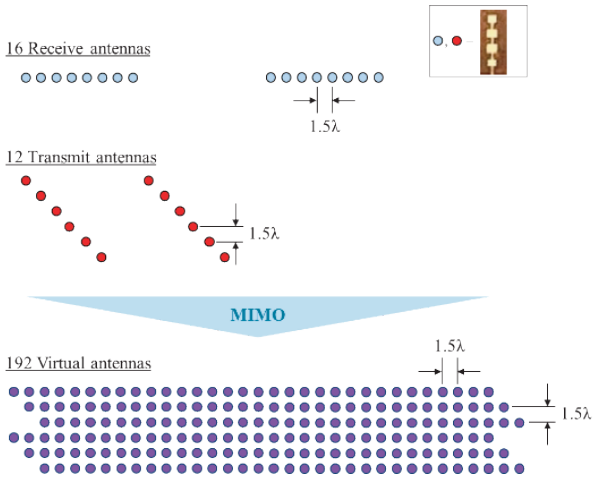

Fig. 4. Array configuration of the in-house developed sparse array radar.

Table 1. Specification of the sparse array radar.

Parameter	Value
Center frequency	78.44 GHz
Bandwidth	1926 MHz
Max. detectable range	35 m
Max. detectable angle	±20° in azimuth
	±13° in elevation
Range resolution	0.16 m
Angular resolution	1.2° in azimuth
	7.5° in elevation
Absolute error	±0.04 m in range
	±0.5° in azimuth

2.3 Measurement setup

To verify the impacts of rainfall on sparse array radars, two measurements were conducted. The first measurement was conducted to verify the impacts of rainfall on the distance detection performance of sparse array radars with the setup shown in Fig. 5a. An aluminum pipe with a diameter of 0.1 m, a length of 0.3 m, and an RCS of 18.7 dBsm was used as a target and placed 10 m in front of the radar. The radar was placed inside a tent, and measurements were conducted without rain directly hitting the radar. The second measurement was conducted to verify the impact on angle detection with the setup shown in Fig. 5b. Two targets were placed at a distance of 10 m in front of the radar so that the angle between the radar and the two targets was 3°. Each measurement was conducted under two conditions: rainfall of 0 mm hr^{-1} and 50 mm hr^{-1}, and the results were compared to verify the impacts of rainfall on the sparse array radar.

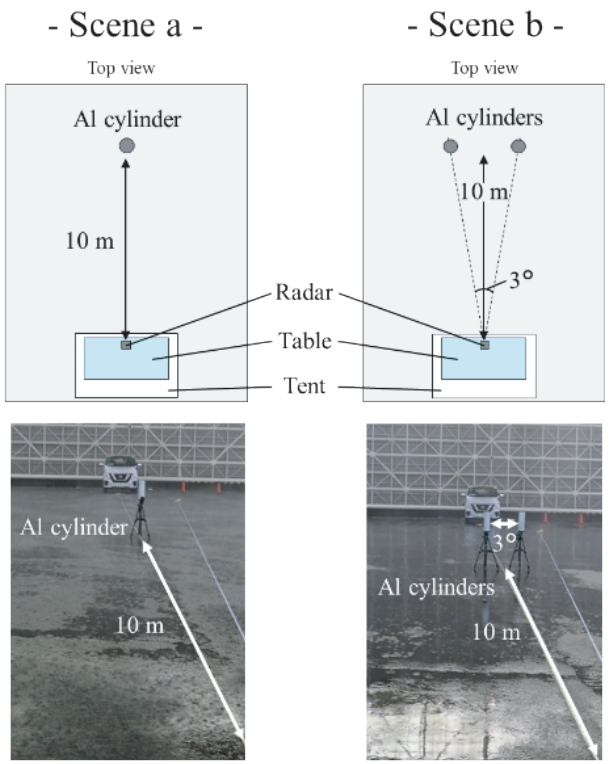

Fig. 5. Measurement setup for verification of the impact on (a) range detection and (b) angle detection.

3. Measurement results

3.1 Impact on range detection

The distance profile obtained from the measurements in Fig. 5a is shown in Fig. 6. The distance profile was obtained by performing range-Doppler FFT on the IF signals acquired by the radar, and then incoherently integrating the distance profiles corresponding to the zero-Doppler of each virtual antenna. To confirm the influence of reflections from the background during measurement, the distance profile obtained when the target was not placed in the rainfall of 0 mm hr $^{-1}$ is also shown in Fig 6. Figure 6 indicates a peak estimated to be from the target was observed at 10.12 m in the distance profile. Comparing the distance profiles at 0 mm hr $^{-1}$ and 50 mm hr $^{-1}$, the peak at 50 mm hr $^{-1}$ was 1.1 dB smaller. The smaller peak is due to rain-induced attenuation when millimeter-wave signals propagate in a rainy environment. On the other hand, no change in the detection position of the peak top was observed between 0 mm hr $^{-1}$ and 50 mm hr $^{-1}$, and no change in the peak top position was observed even when repeated measurements were performed (Table 2).

The 2D imaging results (heat maps) obtained from the measurements in Fig. 5a are shown in Fig. 7. The imaging results were obtained by performing FFT-based DOA estimation process on the results after range-Doppler FFT. The intensity was normalized with the maximum value of the imaging results at 0 mm hr $^{-1}$. Comparing the two imaging results, no significant performance degradation was observed despite the difference in rainfall intensity of 50 mm hr $^{-1}$. Also, no significant differences were observed in the detection positions of the target in the distance direction between the two results, suggesting that the influence of rainfall on distance detection is within the system error of ±4 cm. From the results, since no significant differences in distance detection due to rainfall were observed in both the distance profile and 2D imaging results, it is suggested that the sparse array radar is not significantly affected by rainfall in terms of distance detection.

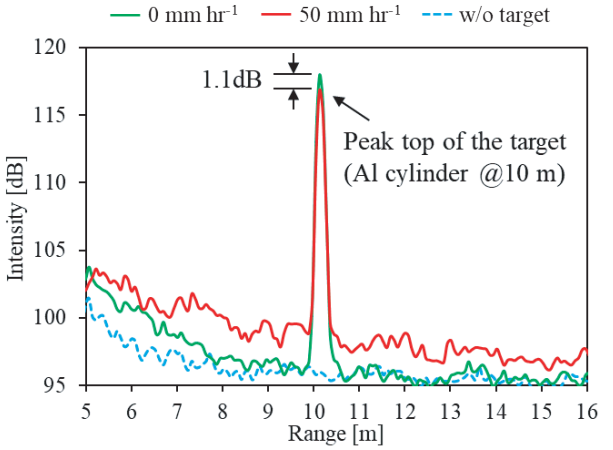

Fig. 6. Range profile of the measurements at (green solid line) 0 mm hr $^{-1}$, (red solid line) 50 mm hr $^{-1}$ and (blue dashed line) without target.

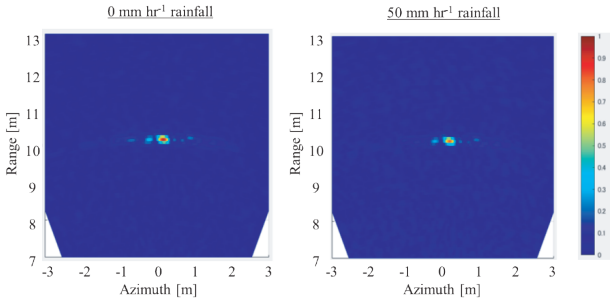

Fig. 7. 2D heatmap of the measurements for the scene a in (left) 0 mm hr $^{-1}$ and (right) 50 mm hr $^{-1}$.

Table 2. Peak-top of several measurements.

Rate of rain [mm hr $^{-1}$]	Iteration	Peak-top [m]
0	1	10.12
	2	10.12
	3	10.12
50	1	10.12
	2	10.12
	3	10.12

3.2 Impact on angle detection

The azimuth profiles obtained from the measurements in Fig. 5b are shown in Fig. 8. The azimuth profiles were extracted from the DOA estimation results for the range bin closest to the target position of 10 m. As in the case of the distance profiles, the azimuth profiles obtained without the target in the rainfall of 0 mm hr $^{-1}$ are also shown in Fig. 8 to confirm the impacts of reflections from the background. From Fig. 8, two peaks with a peak interval of 3.43° were observed in the azimuth profile, and these peaks are estimated to be peaks from the target. Comparing the results for 0 mm hr $^{-1}$ and 50 mm hr $^{-1}$, the peaks are smaller for 50 mm hr $^{-1}$, which is considered to be due to the same reason as the attenuation observed in the distance profile. Additionally, repeated measurements were conducted for the measurements in Fig. 5b, and no measurable degradation were observed in the peak top detection intervals between 0 mm hr $^{-1}$ and 50 mm hr $^{-1}$ (Table 3). The 2D imaging results (heat map) obtained from the measurements in Fig. 5b are shown in Fig. 9. The imaging results were created using the same method as for the distance detection verification. Comparing the two imaging results, no significant performance degradation was observed in the results for rainfall of 50 mm hr $^{-1}$. No clear differences were observed in the azimuth detection positions of the targets between the two cases, suggesting that the influence of rainfall on angle detection is within the system error of ±0.5°. Based on the above, since no significant differences due to rainfall were observed in both the azimuth profile and 2D imaging results, it is suggested that the sparse array radar is not significantly affected by rainfall in terms of angle detection.

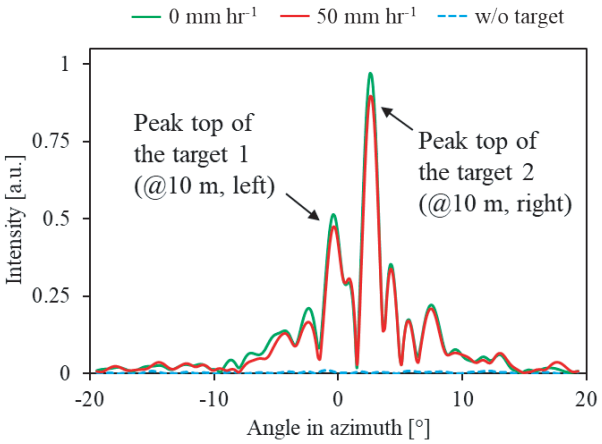

Fig. 8. Azimuth profile of the measurements at (green solid line) 0 mm hr $^{-1}$, (red solid line) 50 mm hr $^{-1}$ and (blue dashed line) without target.

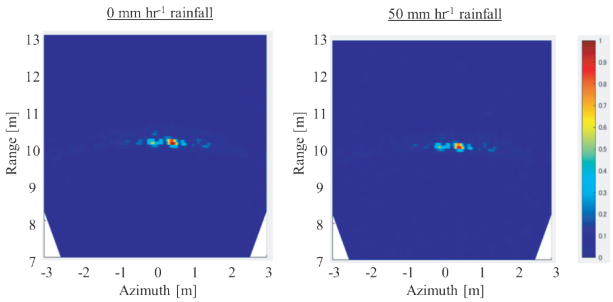

Fig. 9. 2D heatmap of the measurements for the scene b in (left) 0 mm hr $^{-1}$ and (right) 50 mm hr $^{-1}$.

Table 3. Angles between the peak-tops of several measurements.

Rate of rain [mm hr $^{-1}$]	Iteration	Peak-top [m]
0	1	3.43
	2	3.43
	3	3.43
50	1	3.43
	2	3.43
	3	3.43

4. Conclusion

In this study, the impacts of rainfall on the sensing results of a sparse array radar were experimentally verified. The measurements were conducted using the in-house developed sparse array radar in the rain chamber which is capable of imitating the particle size distribution of natural rainfall. The results of the verification indicated an absence of degradation in the distance detection or angle detection, even in conditions of heavy rainfall, with a rainfall rate of 50 mm hr $^{-1}$. The results imply that sparse array radars have the potential to contribute to a high-resolution millimeter-wave radar imaging system that is suitable for outdoor environments.

References

1) C. Waldschmidt, J. Hasch, and W. Menzel, “Automotive radar — from first efforts to future systems,” IEEE Journal of Microwaves, vol. 1, no. 1, pp. 135–148, 2021.
2) M. Byeon and S. W. Yoon, "Analysis of Automotive Lidar Sensor Model Considering Scattering Effects in Regional Rain Environments," in IEEE Access, vol. 8, pp. 102669-102679, 2020.
3) T. Brophy et al., "A Review of the Impact of Rain on Camera-Based Perception in Automated Driving Systems," in IEEE Access, vol. 11, pp. 67040-67057, 2023.
4) A. Meta, P. Hoogeboom and L. P. Ligthart, "Signal Processing for FMCW SAR," in IEEE Transactions on Geoscience and Remote Sensing, vol. 45, no. 11, pp. 3519-3532, Nov. 2007.
5) R. Z. Syeda, T. G. Savelyev, M. C. van Beurden and A. B. Smolders, "Sparse MIMO Array for Improved 3D mm- Wave Imaging Radar," 2020 17th European Radar Conference (EuRAD), Utrecht, Netherlands, 2021, pp. 342-345.
6) G. Schnoering, T. Kawaguchi and C. Höller, "Mixed Near-and Far-Field 2D Imaging with Sparse Arrays," 2024 IEEE Radar Conference (RadarConf24), Denver, CO, USA, 2024.
7) X. Li, X. Wang, Q. Yang, and S. Fu, “Signal processing for TDM MIMO FMCW millimeter-wave radar sensors,” IEEE Access, vol. 9, pp. 167 959–167 971, 2021.
8) I. Bilik, O. Longman, S. Villeval and J. Tabrikian, "The Rise of Radar for Autonomous Vehicles: Signal Processing Solutions and Future Research Directions," in IEEE Signal Processing Magazine, vol. 36, no. 5, pp. 20-31, Sept. 2019.
9) D. Mateos-Núñez, M. A. González-Huici, R. Simoni, F. B. Khalid, M. Eschbaumer and A. Roger, "Sparse array design for Automotive MIMO Radar," 2019 16th European Radar Conference (EuRAD), Paris, France, 2019, pp. 249-252.
10) S. Sun and A. P. Petropulu, "A Sparse Linear Array Approach in Automotive Radars Using Matrix Completion," ICASSP 2020 - 2020 IEEE International Conference on Acoustics, Speech and Signal Processing (ICASSP), Barcelona, Spain, 2020, pp. 8614-8618.
11) C. Schuessler, M. Hoffmann and M. Vossiek, "Super-Resolution Radar Imaging With Sparse Arrays Using a Deep Neural Network Trained With Enhanced Virtual Data," in IEEE Journal of Microwaves, vol. 3, no. 3, pp. 980-993, July 2023.
12) C. Waldschmidt, J. Hasch and W. Menzel, "Automotive Radar — From First Efforts to Future Systems," in IEEE Journal of Microwaves, vol. 1, no. 1, pp. 135-148, Jan. 2021.
13) B. Yektakhah and K. Sarabandi, "Physics-Based Coherent Modeling of Long-Range Millimeter-Wave Propagation and Scattering in Rain," in IEEE Open Journal of Antennas and Propagation, vol. 4, pp. 588-601, 2023.
14) National Research Institute for Earth Science and Disaster Resilience (NIED), “Large-scale Rainfall Simulator,” NIED website, https://www.bosai.go.jp/e/facilities/rainfall.html (accessed Feb. 2025).
15) Marshall, J.S. and Palmer, W.M.K. “The Distribution of Raindrops with Size,” Journal of Meteorology, 5, 165-166, 1948.